Parametrically excited star-shaped patterns at the interface of binary Bose-Einstein condensates

D. K. Maity , K. Mukherjee , 1,2,* S. I. Mistakidis , 2 S. Das , P. G. Kevrekidis, 3,4 S. Majumder , and P. Schmelcher, and P. Schmelcher, ¹Department of Physics, Indian Institute of Technology Kharagpur, Kharagpur 721302, India ²Center for Optical Quantum Technologies, Department of Physics, University of Hamburg, Luruper Chaussee 149, 22761 Hamburg Germany

³Department of Mathematics and Statistics, University of Massachusetts Amherst, Amherst, Massachusetts 01003-4515, USA ⁴Mathematical Institute, University of Oxford, Oxford OX2 6GG, United Kingdom

⁵The Hamburg Centre for Ultrafast Imaging, University of Hamburg, Luruper Chaussee 149, 22761 Hamburg, Germany

(Received 1 May 2020; revised 11 August 2020; accepted 12 August 2020; published 14 September 2020)

A Faraday-wave-like parametric instability is investigated via mean-field and Floquet analysis in immiscible binary Bose-Einstein condensates. The condensates form a so-called ball-shell structure in a two-dimensional harmonic trap. To trigger the dynamics, the scattering length of the core condensate is periodically modulated in time. We reveal that in the dynamics the interface becomes unstable towards the formation of oscillating patterns. The interface oscillates subharmonically, exhibiting an m-fold rotational symmetry that can be controlled by maneuvering the amplitude and the frequency of the modulation. Using Floquet analysis we are able to predict the generated interfacial tension of the mixture and derive a dispersion relation for the natural frequencies of the emergent patterns. A heteronuclear system composed of ⁸⁷Rb - ⁸⁵Rb atoms can be used for the experimental realization of the phenomenon, yet our results are independent of the specifics of the employed atomic species and of the parameters such as scattering lengths and trap strengths at which the driving is applied.

DOI: 10.1103/PhysRevA.102.033320

I. INTRODUCTION

Liquid drops or puddles [1,2] that are weakly affixed to a vertically oscillating surface or a periodically driven spherical liquid drop levitated from the surface, either acoustically [3] or magnetically [4], can display star-shaped patterns. These patterns constitute a paradigm of a spatial as well as temporal symmetry-breaking phenomenon. Their appearance in the form of the so-called Faraday pattern dates back to 1831 for a fluid in a vertically shaken vessel [5]. Very similarly to the original Faraday experiment, the symmetry-breaking instabilities have been intensively studied in classical fluids considering a variety of surfaces of the liquid such as spherical [6,7], cylindrical [8,9], and flat [10,11]. Remarkably, the dominant wavelength of the instability and the symmetries of the emergent patterns are determined by a few intrinsic properties such as the density and the surface tension of the liquid [12,13].

Over the last two decades, Bose-Einstein condensates (BECs), due to their remarkable experimental tunability [14–16], have facilitated the investigation of various classical hydrodynamical instabilities in the context of quantum fluids. Indeed, several theoretical works unveiled the emergence of parametric resonances [17] and Faraday waves [18–20], either via confinement modulations [21,22] or by means of a time-dependent scattering length [18], inspiring also the experimental realization of parametric resonances [23] and Faraday waves in BECs [24,25].

Importantly, even though such modulation dynamics has been extensively unraveled for single-component BECs [17,18,22,26–32], the corresponding two-dimensional (2D) multispecies BEC scenario is far less explored [33–37]. In this context, multispecies BECs exhibiting a well-defined interface [38-41] can emulate some of the well-known interfacial-tension-dominated fluid instabilities. These include the Rayleigh-Taylor [42–44], the capillary [45,46], the Kelvin-Helmholtz [47–49], the Richtmyer-Meshkov [50], the countersuperflow [51-54], and the Rosensweig instability [55] as well as the Bénard-von-Kármán vortex street [56,57] and quantum swapping of the involved immiscible condensates [58,59]. The interface dynamics of weakly immiscible BECs has also been studied by means of a variational approach [43], deriving a dispersion relation for the emergent instabilities for different types of driving forces, including stochastic ones. In fact the parametric resonance of capillary waves leading to the generation of vortex-antivortex pairs at the interface of two immiscible ribbonlike condensates, under the action of a high-amplitude oscillating force that pushes the condensates towards each other, has been explored in Ref. [60]. A particular feature of that work consists of the ribbonlike geometry enabling a transverse interface separating the two elongated condensates, and the parametric instability consists of the amplification of the associated transverse Fourier modes. Recall that for multispecies BECs the interfacial tension stems from the combined effect of pressure and interspecies interactions [46,61,62]. Interestingly, harmonically trapped quasi-2D binary condensates can form a circular interface between them, rendering these systems ideal candidates to probe azimuthal symmetry-breaking

^{*}koushikphysics21@gmail.com

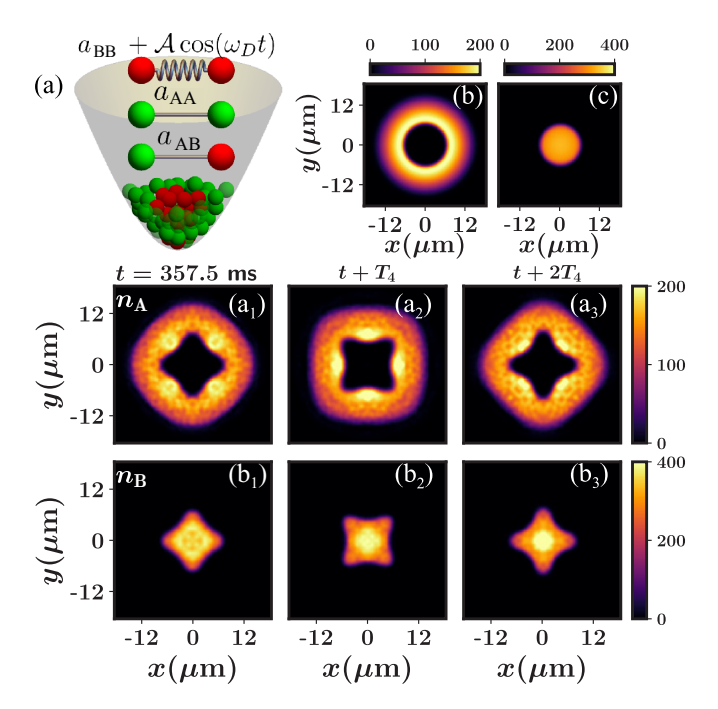


FIG. 1. (a) Schematic representation of the 2D harmonically trapped binary BEC and the modulation protocol. Density profiles of (b) species A and (c) species B in the initial state where the intra- and the interspecies scattering lengths are $a_{AA} = 99a_B$, $a_{BB} = 75a_B$, and $a_{AB} = 213a_B$. Snapshots of the density profiles of (a_1-a_3) species A and (b_1-b_3) species B at consecutive periods nT_4 of the modulation (see legend). The ${}^{87}\text{Rb} - {}^{85}\text{Rb}$ binary BEC consisting of $N_A = 10^4$ and $N_B = 5 \times 10^3$ atoms is prepared as in Figs. 1(b) and 1(c). The dynamics is initiated following a periodic modulation of a_{BB} at frequency $\omega_D/(2\pi) = 1/T_4 = 69$ Hz and amplitude $\mathcal{A} = 15a_B$. The star-shaped pattern D_4 exhibits four lobes; see also Supplemental Material Ref. [65] for videos of the dynamics.

instabilities. The analogs of the latter in classical fluids are extremely useful in experiments [1,2,13] for determining the surface tension of the liquid. Therefore, it would be extremely desirable to explore whether interfacial pattern formation in 2D binary BECs can provide information regarding the interfacial tension of the mixture.

In this work, we propose a parametrically driven mechanism that enables on-demand azimuthal-mode pattern formation at the interface between two immiscible BECs. This, on the one hand, lends further support to the striking similarity of a number of features shared by the classical fluid and the BEC systems and, on the other hand, paves the way to determining the interfacial tension in ultracold-atom experiments based on the resulting patterns occurring at the interface among the components. More specifically, we consider a binary BEC of two different atomic species confined in a 2D axisymmetric harmonic trap [see Fig. 1(a)] and interacting via short-range repulsive interactions. The mixture is initialized in a radially symmetric, phase-separated configuration [63,64], where the species with weaker interactions is surrounded by the one with stronger interactions, thus forming a so-called ball-shell structure with a circularly symmetric interface [Figs. 1(b)] and 1(c)].

Upon applying a time-periodic modulation of the intraspecies core-component interaction we demonstrate that both the spatial and the temporal symmetries of the interface are broken. Importantly, depending on the modulation strength and frequency, star-shaped density patterns D_m , with underlying m-fold rotational symmetry, appear at the interface which oscillates subharmonically, i.e., at half the modulation frequency. To elucidate the emergence of the resulting patterns, the underlying mean-field equations are reduced to a Mathieu equation at the level of the amplitude of the mth mode, where Floquet theory is subsequently applied. A dispersion relation relating the azimuthal wave number m of the pattern to its frequency ω_m is derived. The stability boundaries of the resulting star-shaped patterns are identified at the level of the full mean-field model, being in good agreement with the predictions of the effective theoretical analysis in terms of the Floquet theory. Remarkably, it is demonstrated that this dispersion relation can be employed to predict the interfacial tension of the phase-separated BEC. To generalize our findings, we showcase that the generation of the star-shaped patterns can also be achieved for strongly mass-imbalanced mixtures or by considering other driving protocols such as a periodic modulation of the core-component harmonic trap.

Our presentation is structured as follows. Section II introduces the relevant theoretical framework, the employed driving protocol, and the experimentally relevant parameters of our setup. In Sec. III we discuss the emergence of star-shaped patterns following a periodic driving of the core-component scattering length and derive a dispersion relation for the observed patterns. The generation of star-shaped patterns upon considering a periodic modulation of the core-component harmonic trap is demonstrated in Sec. IV. Section V presents the occurrence of pattern formation for strongly mass-imbalanced binary BECs. In Sec. VI we summarize and provide an outlook of future perspectives. Appendix A further elaborates on the details of the utilized mean-field framework and the ingredients of the presented simulations. In Appendix B we showcase the robustness of the pattern formation for periodic modulations of the shell condensate scattering length and in Appendix C we provide a detailed derivation of the corresponding Mathieu equation characterizing the deformation of the intercomponent interface.

II. MODEL AND DRIVING PROTOCOL

Our theoretical approach to describe the dynamics of the binary BEC relies on the coupled system of time-dependent Gross-Pitaevskii (GP) equations [66,67]

$$i\hbar \frac{\partial}{\partial t} \Psi_{j}(\mathbf{r}, t)$$

$$= \left\{ -\frac{\hbar^{2}}{2m_{j}} \left[\frac{1}{r} \frac{\partial}{\partial r} \left(r \frac{\partial}{\partial r} \right) + \frac{1}{r^{2}} \frac{\partial^{2}}{\partial \theta^{2}} + \frac{\partial^{2}}{\partial z^{2}} \right] + \frac{1}{2} m_{j} \omega_{j}^{2} \left(r^{2} + \lambda_{j}^{2} z^{2} \right) + g_{jj} |\Psi_{j}|^{2} + g_{jj'} |\Psi_{j'}|^{2} \right\} \Psi_{j}(\mathbf{r}, t).$$

$$(1)$$

Here, $\mathbf{r} \equiv (r, \theta, z)$ denotes the cylindrical coordinates, $j, j' \in (A, B)$, and the wave function Ψ_j of species j satisfies

 $\int |\Psi_i|^2 d\mathbf{r} = N_i$. Also, N_i , m_i , and ω_i denote the atom number, the mass, and the transverse harmonic trap frequency of species j, respectively. The parameter λ_i is the ratio of the axial and the transverse trap frequencies of species j satisfying here $\lambda_i = \omega_{zi}/\omega_i \gg 1$, which ensures that the dynamics in the z direction is "frozen out," The intra- and interspecies interaction strengths g_{AA}, g_{BB}, and g_{AB} satisfy the so-called phase-separation condition defined as K = $g_{AB}g_{BA}/(g_{AA}g_{BB}) \propto a_{AB}^2/(a_{AA}a_{BB}) \geqslant 1$ [68,69], where a_{jj} and $a_{ii'}$ are the corresponding s-wave scattering lengths. In particular, the mixture is characterized as weakly immiscible if K is slightly larger than unity but $K \to 1$, while it is perfectly immiscible if $1/K \rightarrow 0$ [61]. Equation (1) is solved using a split-time Crank-Nicolson method [70,71] in imaginary time to obtain the initial ground state, and in real-time to monitor the dynamics, in two dimensions, characterized by the wave functions $\psi_i(r,\theta)$ [72]. For details on the dynamical reduction from three to two dimensions in Eq. (1) (see Appendix A). With the initial state at hand, we trigger the interfacial dynamics of the binary BEC by periodically modulating the scattering length a_{BB} according to

$$\tilde{a}_{\rm BB}(t) = a_{\rm BB} + \mathcal{A}\cos(\omega_D t),\tag{2}$$

where \mathcal{A} and ω_D are the amplitude and frequency of the modulation.

The experimentally relevant parameters of a ⁸⁷Rb - ⁸⁵Rb binary BEC, in the hyperfine states $|F=1, m_F=-1\rangle$ and $|F=2, m_F=-2\rangle$, respectively, labeled species A and species B, are utilized. Namely, $\omega_A/2\pi = \omega_B/2\pi \equiv \omega/2\pi =$ 15 Hz, $N_A = 10^4$, $N_B = 5 \times 10^3$, $a_{AA} = 99a_B$, and $a_{AB} = 99a_B$ $213a_{\rm B}$, with $a_{\rm B}$ being the Bohr radius [64]. Accordingly, the initial state corresponds to a shell-structured geometry in which ⁸⁵Rb atoms occupy the central region of the trap [Fig. 1(c)] and hence are referred to as the core condensate, while ⁸⁷Rb atoms form a lower-density shell [Fig. 1(b)] surrounding the core condensate. Note that for this choice of interactions $K \approx 2.47$, and hence the mixture can be considered to reside deeply in the immiscible phase. Since the scattering length $a_{\rm BB}$ can be experimentally tuned via a Feshbach resonance in the range of $50a_B$ – $900a_B$ [64], we periodically vary $a_{\rm BB}$ in time around $a_{\rm BB}=75a_{\rm B}$, which ensures that the phaseseparated condition is fulfilled throughout the dynamics.

We note that the interspecies Feshbach resonances of the heteronuclear ⁸⁷Rb - ⁸⁵Rb gas are located far away from the corresponding Feshbach resonance of the 85Rb $|F=2, m_F=-2\rangle$ state [73,74]. Also, to the best of our knowledge, no Feshbach resonance has been reported yet for the state $|F=1, m_F=-1\rangle$ of ⁸⁷Rb [75]. Thus, the modulation of the scattering length $a_{\rm BB}$ can be carried out without altering (at least up to a good degree) the scattering lengths a_{AB} and a_{AA} . Moreover, a modulating magnetic field near a Feshbach resonance can be used to realize the periodic driving of the scattering length $a_{\rm BB}$ as in the experiment in Ref. [76], where the design of specific waveforms is showcased with the aid of a waveform generator. In particular, as a case example we use a modulation amplitude $A = 15a_B$; for variations of this parameter see also the discussion below. This driving process leads, in the long-time dynamics, to the formation of patterns at the interface which steadily oscillates at half the

modulation frequency. Importantly, the observed pattern formation occurs also for atomic species different from the ones considered herein or hyperfine states of the same isotope, e.g., for the $|F=1,m_F=-1\rangle$ and $|F=2,m_F=+1\rangle$ hyperfine states of ⁸⁷Rb [77]). Moreover, it takes place irrespectively of the periodic driving of the involved intra- or interspecies scattering lengths. Therefore, it represents a *generic* phenomenology of the immiscible two-component system; see also the discussion in Sec. V and in Appendix B.

III. PERIODIC DRIVING OF THE CORE-COMPONENT SCATTERING LENGTH

Below, we expose the generation of star-shaped patterns upon applying time-periodic modulation of the core-component scattering length as introduced in Eq. (2). In particular, we first quantify the emergence of the star-shaped patterns within the mean-field framework (Sec. III A). Subsequently, a dispersion relation predicting the natural frequencies of the observed patterns is derived using Floquet theory (Sec. III B).

A. Pattern formation in the mean-field dynamics

Representative density profiles of each species, $n_i = |\psi_i|^2$, unveiling the dynamical generation of a star-shaped pattern D_4 with m=4 lobes at instants in time representing integer multiples of the modulation period T_4 are illustrated in Fig. 1 following a periodic oscillation of $a_{\rm BB}$ with $\omega_D/2\pi =$ 69 Hz. It becomes apparent that the four-lobed star pattern [Figs. $1(a_1)$ and $1(b_1)$] dynamically appears at the interface at t = 357.5 ms for the first time. Indeed, the instability in the system grows until it is clearly visible in the density profiles after about 357.5 ms. The exact same structure reappears at time $t + 2T_4$ [Figs. 1(a₃) and (b₃)], thus revealing its subharmonic nature. Note that the lobes of the D_4 pattern at $t = T_4$ are oriented in a way rotated by an angle $\pi/4$ with respect to the one at t = 357.5 ms or $t + 2T_4$ [Figs. 1(a₂) and $1(b_2)$]. Importantly, patterns with higher *m*-fold rotational symmetries can also be dynamically generated. To achieve this we fix the modulation amplitude at $A = 15a_B$ and change the modulation frequency ω_D . As we explain later, a certain symmetric pattern D_m is realized within a specific interval of ω_D for a given amplitude \mathcal{A} , while outside this interval the pattern disappears. Prototypical examples of relevant density profiles for symmetric patterns D_3 , D_5 , D_6 , and D_7 with three, five, six, and seven lobes realized at modulation frequencies $\omega_D \approx 48$ Hz, $\omega_D \approx 95.1$ Hz, $\omega_D \approx 132$ Hz, and $\omega_D \approx 157.5$ Hz, respectively, are depicted in Fig. 2. Indeed, the same density pattern D_m is repeated, but with a different orientation (at an angle π/m) compared to the earlier one, after every single period of the modulation.

To expose the nature of the interfacial dynamics, we next perform a linear stability analysis based on the Floquet technique [11,18,78–80], by assuming that both species possess a uniform density with a sharp boundary between them. Indeed, within the GP calculations we observe that the BEC background density undergoes only a small amplitude breathing motion. This allows us to neglect the effect of local density fluctuations within the stability analysis. We further presume

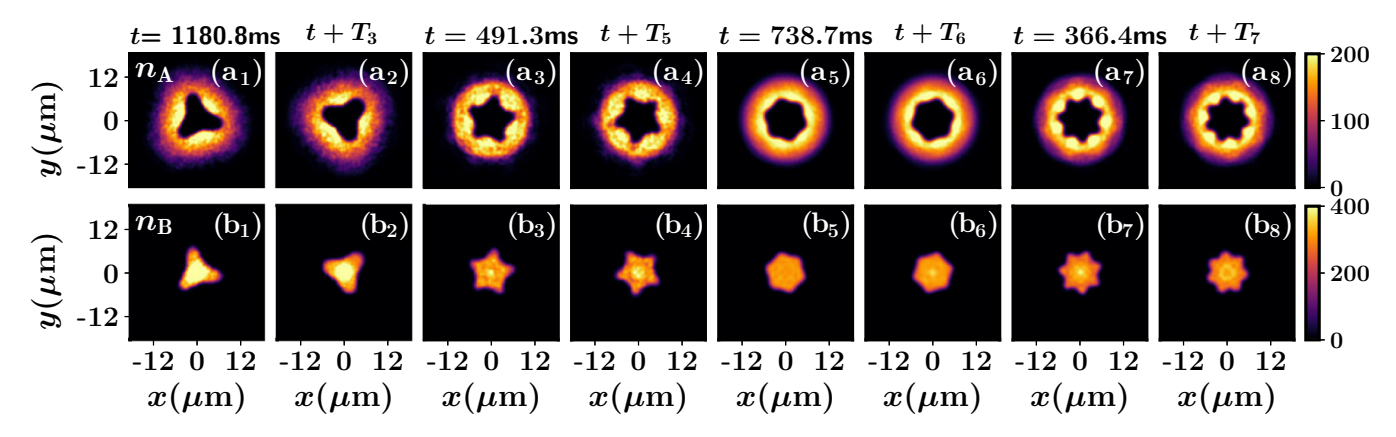


FIG. 2. Density profiles of (a_1-a_8) species A and (b_1-b_8) species B for various symmetric patterns, D_3 [(a_1) , (a_2) , (b_1) , (b_2)], D_5 [(a_3) , (a_4) , (b_3) , (b_4)], D_6 [(a_5) , (a_6) , (b_5) , (b_6)], and D_7 [(a_7) , (a_8) , (b_7) , (b_8)], at specific instants in time (see legends) in the long-time dynamics. T_m is the driving period corresponding to the m-fold symmetric pattern D_m , which is generated by periodically modulating the scattering length $a_{\rm BB}$ in time with amplitude $\mathcal{A}=15a_{\rm B}$ and frequency $\omega_D=2\pi/T_m$; see also Supplemental Material Ref. [65] for videos of the dynamics. The $^{87}{\rm Rb}$ - $^{85}{\rm Rb}$ binary BEC consists of $N_{\rm A}=10^4$ and $N_{\rm B}=5\times10^3$ atoms initially prepared as in Fig. 1.

that the same interface dynamics can be retrieved following the periodic modulation of any other prototypical system parameter (i.e., the different scattering lengths or trap strengths), since the natural angular frequencies of the interfacial patterns should be independent of the parameter at which the periodic protocol is applied. In fact, we have confirmed that it is possible to generate all the different *m*-fold symmetric patterns also for a weakly immiscible $(K \to 1)^{87} \text{Rb} - ^{85} \text{Rb}$ mixture. Most importantly, in the latter scenario, the individual star-shaped patterns possess lower natural angular frequencies compared to the deeply immiscible case. We also remark that for larger values of the modulation amplitude, e.g., $A = 38a_B$, we do not typically observe the generation of (long-lived) vortical patterns in the spirit of Ref. [60]. Instead, the above-described symmetric patterns can still be formed at the initial stages of the periodically driven dynamics and subsequently disappear for longer evolution times. This phenomenon is attributed to the fact that the high driving amplitude induces a large amount of incoherent excitations into the system. Moreover, in this setting, it is reasonable to expect that the system dynamics lies beyond the applicability of the mean-field approximation. For these reasons, we do not pursue the high-amplitude excitation regime further in the present study.

B. Dispersion relation and stability boundaries of the patterns within Floquet theory

To this end, for the convenience of the theoretical analysis a time-dependent harmonic potential of the core condensate is considered instead of the periodic driving of its scattering length. The adjustable nature of both the trapping potential and the scattering length by means of a tunable magnetic field in typical BEC experiments [14,81,82] supports this assumption further, at least for predicting the natural frequencies of the interface patterns.

For simplicity we again start our analysis in three dimensions and subsequently reduce the problem to two dimensions. It is appropriate to express the condensate wave function according to the Madelung transformation [83], i.e.,

 $\Psi_j(r,\theta,z) = \sqrt{n_j(r,\theta,z)}e^{i\phi_j}$, where n_j and ϕ_j are the density and the phase of species j. Correspondingly, the superfluid velocity $\mathbf{v}_j = (v_{jr}, v_{j\theta}, v_{jz})$ is defined as $\mathbf{v}_j = \frac{\hbar}{m_j} \nabla \phi_j$, where ϕ_j is also known as the velocity potential [84]. Furthermore, it is reasonable to approximate $n_A = 0$ for r < R and $n_B = 0$ for r > R, with R being the radius of the interface. Therefore, the coupled GP system of Eq. (1) can be expressed in the form [84]

$$-m_j \frac{\partial \mathbf{v}_j}{\partial t} = \frac{\nabla P_j}{n_i}, \quad \nabla^2 \phi_j = 0. \tag{3}$$

The effective pressure term of the individual species is $P_{\rm A} = \frac{1}{2} (m_{\rm A} n_{\rm A} v_{\rm A}^2) + \frac{\hbar^2 \sqrt{n_{\rm A}}}{2m_{\rm A}} \nabla^2 \sqrt{n_{\rm A}} + g_{\rm AA} n_{\rm A}^2 + \frac{1}{2} m_{\rm A} n_{\rm A} \omega^2 (r^2 + r^2)$ $\lambda_{\rm A}^2 z^2$) and $P_{\rm B} = \frac{1}{2} (m_{\rm B} n_{\rm B} v_{\rm B}^2) + \frac{\hbar^2 \sqrt{n_{\rm B}}}{2m_{\rm B}} \nabla^2 \sqrt{n_{\rm B}} + g_{\rm BB} n_{\rm B}^2 +$ $\frac{1}{2}m_{\rm B}n_{\rm B}\omega^2(r^2+\lambda_{\rm B}^2z^2)+\frac{1}{2}m_{\rm B}n_{\rm B}\omega^2r^2b\cos(\omega_Dt)),$ tively. Note that the problem has been effectively reduced to two single-component problems interacting through their sharp interface. The influence of g_{AB} is still implicitly incorporated in the values of R, $n_{\rm B}$, and n_A taken from the full GP model. Importantly, here, the amplitude b is related to \mathcal{A} (at the GP level) by $b = 8\pi \hbar^2 \mathcal{A} |\Psi_{\rm B}(r = R, \theta, z)|^2 / (m_{\rm B}^2 \omega^2 R^2).$ This is derived in order to have the same dynamical impact on the interface by both protocols; i.e., it is obtained by equating the corresponding modulation terms at the interface r = R, namely, $4\pi \hbar^2 A \cos(\omega_D t) |\Psi_B|^2 \Psi_B / m_B =$ $(1/2)m_{\rm B}\omega^2R^2b\cos(\omega_Dt)\Psi_{\rm B}$. After the onset of the instability, the interface is deformed by a small amount ζ . The stress balance condition (also known as Laplace's formula in fluid mechanics) at the interface can be written as [45,85]

$$[P_{\rm B} - P_{\rm A}]_{r=R+\zeta} = \sigma \left[\frac{1}{R_1} + \frac{1}{R_2} \right],$$
 (4)

where R_1 and R_2 are the principal radii of the interface curvature and σ denotes the interfacial tension. Linearizing Eq. (4) in terms of the interface deformation amplitude ζ and

using Eq. (3) we get [85]

$$\left(\hbar n_{\rm A} \frac{\partial \phi_{\rm A}}{\partial t} - \hbar n_{\rm B} \frac{\partial \phi_{\rm B}}{\partial t}\right)_{|_{r=R}} = -R m_{\rm B} \omega^2 n_{\rm B} b \cos(\omega_D t) \zeta
- \sigma \left(\frac{1}{R^2} + \frac{1}{R^2} \frac{\partial^2}{\partial \theta^2} + \frac{\partial^2}{\partial z^2}\right) \zeta.$$
(5)

Here, nonlinear terms like v_j^2 and quantum pressure $(\sim \sqrt{n_j} \nabla^2 \sqrt{n_j})$ are neglected, and we assume $m_A \approx m_B$ owing to the presence of a very small mass imbalance in our system. The kinematic boundary condition is [85]

$$\frac{\partial \zeta}{\partial t} = v_{\rm Ar}(r = R) = v_{\rm Br}(r = R). \tag{6}$$

Utilizing Eqs. (3) and (6), the interface deformation and the velocity potentials can be expressed as

$$\zeta(\theta, z, t) = \sum_{m=1}^{\infty} \zeta_m(t) e^{i(m\theta + kz)},$$

$$\phi_{A}(r, \theta, z, t) = \sum_{m=1}^{\infty} \frac{d\zeta_m(t)}{dt} \frac{m_{A}K_m(kr)}{\hbar k K'_m(kR)} e^{i(m\theta + kz)},$$

$$\phi_{B}(r, \theta, z, t) = \sum_{m=1}^{\infty} \frac{d\zeta_m(t)}{dt} \frac{m_{B}I_m(kr)}{\hbar k I'_m(kR)} e^{i(m\theta + kz)}.$$

Here, $I_m(kr)$ and $K_m(kr)$ denote the mth-order modified Bessel functions [86] of the first and second kind, respectively, while the integers m and k represent the azimuthal and axial wave numbers, respectively. Substituting the expansions of $\zeta(r, \theta, z)$, $\phi_A(r, \theta, t)$, and $\phi_B(r, \theta, z)$ into Eq. (5) and considering $k \to 0$ (no wave excitation along the z direction) we arrive at a Mathieu-type equation (see also Appendix C) for ζ_m , namely,

$$\ddot{\zeta}_m + \omega_m^2 [1 - (b/b_{0m})\cos(\omega_D t)] \zeta_m = 0, \tag{7}$$

with $\omega_m^2 = \frac{\sigma}{R^3} \frac{m(m^2-1)}{(m_B n_B - m_A n_A)}$ and $b_{0m} = \frac{\sigma(m^2-1)}{m_B \omega^2 n_B R^3}$. Remarkably, the expression of the natural frequency ω_m (dispersion relation) has the same form as that of a classical inviscid incompressible fluid [12,87]. Indeed, the above dispersion relation is able to qualitatively capture the basic features of the pattern formation. For instance, it evinces that higher-fold symmetric patterns can be realized for higher driving frequencies. According to Floquet theory, there exists a solution $\zeta_m(t) = e^{(s+i\alpha\omega_D)t} \sum_{p=-\infty}^{\infty} \zeta_m^{(p)} e^{ip\omega_D t}$, where s is the growth rate and α is the Floquet exponent. Inserting this into Eq. (7), the Floquet expansion of ζ_m leads to a linear difference equation,

$$A_m^{(p)}\zeta_m^{(p)} = b(\zeta_m^{(p-1)} + \zeta_m^{(p+1)}), \tag{8}$$

with $A_m^{(p)} = [-2(p+\alpha)^2 \omega_D^2 \frac{(m_B n_B - m_A n_A)}{m m_B \omega^2 n_B} + \frac{2\sigma(m^2-1)}{R^3 n_B m_B \omega^2}]$. Note that the parameter b, which is the modulation amplitude of the harmonic trap, carries the same meaning in both Eq. (3) and Eq. (8).

The eigenvalues $b(\omega_D, m)$ in Eq. (8), depending on the parameter s, describe the stability of the system in the parameter space of the driving amplitude \mathcal{A} and frequency ω_D . Namely, the system is unstable when s > 0 and pattern formation is expected to occur at the interface. In particular,

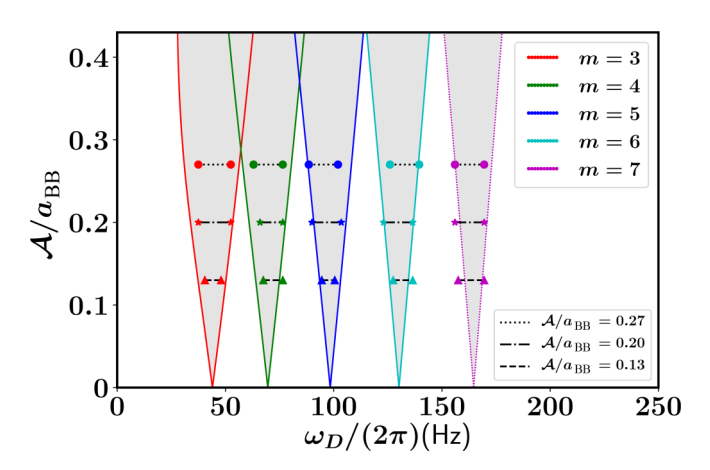


FIG. 3. The marginal stability boundaries, predicted within Floquet theory, for the first subharmonic excitations of different azimuthal wave numbers m. The system is unstable inside the tongues (shaded regions) towards the formation of m-fold star-shaped symmetric patterns D_m . Two starlike (circular) [triangular] data points connected by a dashed (dotted) [dashed-dotted] line within each tongue indicate the frequency interval for the fixed amplitude $\mathcal{A}=0.20a_{\rm BB}$ (0.27 $a_{\rm BB}$) [0.13 $a_{\rm BB}$], where GP calculations have been performed.

we let s=0, which provides the marginal stability boundaries for different values of the azimuthal wave number m (see Fig. 3). Recall that for subharmonically excited waves the relation $\omega_m = \omega_D/2$ holds, which allows us to set $\alpha = 1/2$. In principle, the stability curve is composed of an infinite series of resonant tongues. However, in Fig. 3 we showcase the first subharmonic marginal stability boundaries for m=3, 4, 5, 6, and 7 since those are the ones that we have shown previously in the form of star-shaped patterns in the GP framework. Indeed, the system will be unstable, exhibiting pattern formation, if \mathcal{A} and ω_D lie inside the boundaries of a specific tongue (see, e.g., the stars in Fig. 3) but it is stable when they reside outside these tongues.

To expose the reliability of the predictions of Floquet theory we also present in Fig. 3, with data points, the borders at which pattern formation in terms of ω_D and \mathcal{A} occurs within the GP theory. For instance, we find that for 0.13 <A < 0.27 all different patterns can be realized within the mean-field framework, meaning that only some of the *m*-fold structures cannot be captured for other amplitudes. Another key observation here is that for a fixed A the widths of the stability boundaries in the effective theory appear to decrease for larger ω_D but they show a nonmonotonic behavior in the mean-field calculations (Fig. 3). This deviation (as well as similar nonmonotonicities for fixed ω_D and varying \mathcal{A}) can be attributed to the linear nature of the theoretical model ignoring possible nonlinear effects captured in the GP framework. For instance, in the high-driving-amplitude regime, such as the one with $A/a_{\rm BB} > 0.3$ (Fig. 3), the resonant tongues overlap with each other, indicating that the linear stability analysis is no longer valid. Indeed, the predictions of the effective theory are accurate only for weak modulation amplitudes, herein $A/a_{\rm BB} < 0.3$. Note that the symmetries of the patterns depend crucially on ω_D , i.e., for a larger ω_D higher-fold symmetries appear in the system. Furthermore, recall that the patterns are

repeated after $t + nT_m$, $n = 1, 2, \ldots$, being rotated by $n\pi/m$ with respect to the one at t. This behavior is associated with the spatial and temporal symmetry of the system, which can be explained by the Floquet analysis. For instance, $\zeta(\theta, t) = \sum_{m=1}^{\infty} \zeta_m(t)e^{im\theta}$ is invariant under the transformations $\theta \to \theta + (n\pi/m)$ and $t \to t + nT$, which exactly correspond to the spatial and temporal reprisals of the patterns according to the predictions of the GP calculations. Finally, in order to calculate the interfacial tension [46,61,62], we compare our GP results (\mathcal{A}, ω_D) for a particular symmetric pattern to the instability tongues emerging from the Floquet analysis [Eq. (7)]. This gives a value of the interfacial tension $\sigma = 1.1 \times 10^{-18} \pm 5\%$ N/m [88].

IV. DYNAMICS AFTER A MODULATION OF THE EXTERNAL CONFINEMENT

In the previous section, for the convenience of the Floquet analysis we assumed that the modulation of the scattering length of the core component has the same impact on the interface dynamics of the binary BEC as the one when applying an independent modulation of the external confinement of the core component and keeping the scattering lengths fixed. This is due to the fact that the natural angular frequencies ω_m [see the discussion following Eq. (7)] of the patterns do not depend on whether one of the systems' scattering lengths (see also the discussion in Appendix B) or the external trap frequency (see the description below) is being modulated as long as the corresponding modulation amplitude is low compared to the original value of the perturbed parameter. Furthermore, as can also be verified within the full GP calculations presented in Sec. III A the modulation dominantly affects the interface of the binary BEC where the species densities are vanishing since we operate in the deep immiscible interaction regime. Thus, in principle, it is possible to adjust the modulation amplitudes of the different time-dependent protocols such that the latter produce the same impact on the BEC interface. Along these lines, it is possible to equate the corresponding modulation terms at the interface, which allows us to establish the relation $b = 4N_{\rm B}\sqrt{2\pi\lambda}\mathcal{A}|\psi_{\rm B}|^2/(a_{\rm osc}R^2)$, where $\psi_{\rm B}$ (r=R) is taken from the initial state obtained within the 2D GP framework. Indeed, the latter formula connects the modulation amplitudes of the two dynamical protocols.

To substantiate our above-mentioned argument regarding the same impact of the protocols on the interface, we subsequently solve the 2D GP equations of motion following a modulation of the confinement of the core component while keeping $a_{\rm BB}$ fixed (see Appendix A for the reduction of the GP equations from three to two dimensions). In this case, the corresponding coupled system of GP equations reads

$$i\frac{\partial \psi_{A}(x, y, t)}{\partial t}$$

$$= \left[-\frac{1}{2}\nabla_{\perp}^{2} + \frac{1}{2}(x^{2} + y^{2}) + \sum_{j} \mathcal{G}_{Aj}|\psi_{j}(x, y)|^{2} \right] \psi_{A}(x, y, t)$$

and

$$i\frac{\partial \psi_{B}(x, y, t)}{\partial t}$$

$$= \left[-\frac{m_{r}}{2} \nabla_{\perp}^{2} + \frac{1}{2m_{r}} (x^{2} + y^{2})(1 + b \cos(\omega_{D} t)) + \sum_{j} \mathcal{G}_{Bj} |\psi_{j}(x, y)|^{2} \right] \psi_{B}(x, y, t). \tag{10}$$

In these equations, $\nabla_{\perp}^2 = \partial_x^2 + \partial_y^2$ connects to the kinetic energy term and $m_r = m_{\rm A}/m_{\rm B}$. Furthermore, $\mathcal{G}_{\rm AA} = 2N_{\rm A}\sqrt{2\pi\lambda}a_{\rm AA}/a_{\rm osc}$ and $\mathcal{G}_{\rm BB} = 2m_rN_{\rm B}\sqrt{2\pi\lambda}a_{\rm BB}/a_{\rm osc}$ are the intraspecies interaction strengths, while $\mathcal{G}_{jj'} = N_{j'}(1+m_r)\sqrt{2\pi\lambda}a_{jj'}/a_{\rm osc}$ is the interspecies interaction strength.

To demonstrate the connection with the previously discussed results we consider a 87Rb-85Rb binary BEC with ⁸⁷Rb (⁸⁵Rb) being referred to as species A (B) in the following. Moreover, both species in the system are confined in a 2D harmonic trap with frequencies $\omega_A/2\pi = \omega_B/2\pi \equiv$ $\omega/2\pi = 15$ Hz. The intra- and interspecies scattering lengths are chosen to be $a_{BB} = 75a_B$, $a_{AA} = 99a_B$, and $a_{AB} = 213a_B$, while each species contains a particle number $N_A = 10^4$ and $N_{\rm B} = 5 \times 10^3$, respectively. Consequently, the binary BEC is initially prepared in its ground state, which corresponds to the phase-separated state described by the densities shown in Figs. 1(b) and 1(c). To induce the dynamics we impose a periodic driving on the trapping potential of the core component as described in Eq. (10) with amplitude b and frequency ω_D . Note that the value b = 0.24 is considered herein, which exactly corresponds to the modulation amplitude $A = 15a_{\rm R}$ of the scattering length of the core component examined in Sec. III A.

Figure 4 depicts some representative density profiles of each species at specific instants in time of the long-time dynamics following the above-mentioned driving protocol on the confinement of the core component. As can be readily seen, different symmetric patterns D_m characterized by a respective m-fold symmetry build upon the densities of the individual species after every period of the modulation. For instance, we observe that fivefold [Figs. $4(a_1)-4(a_3)$ and $4(b_1)-4(b_3)$] and sevenfold [Figs. $4(a_4)-4(a_6)$ and $4(b_4)-4(b_6)$] star-shaped patterns are generated for driving frequencies $\omega_D = 96 \text{ Hz}$ and $\omega_D = 165$ Hz, respectively. Remarkably enough, these frequencies lie inside the corresponding resonant tongues obtained within Floquet theory and illustrated in Fig. 3. Importantly, these m-fold star-shaped patterns repeat themselves after a time $t' = t + 2T_m$ and undergo a π/m rotation every $t = T_m$. This behavior essentially manifests the subharmonic feature of the formed patterns, a phenomenon that has also been observed upon applying a modulation of the core-component scattering length discussed in Sec. III A. We remark that also every other m-fold pattern can be created using different driving frequencies of the external confinement of the core component.

Summarizing, we can deduce that the overall phenomenology observed in the interfacial dynamics of the binary BEC is the same when following a periodic modulation of either the scattering or the confinement of the core component. As a

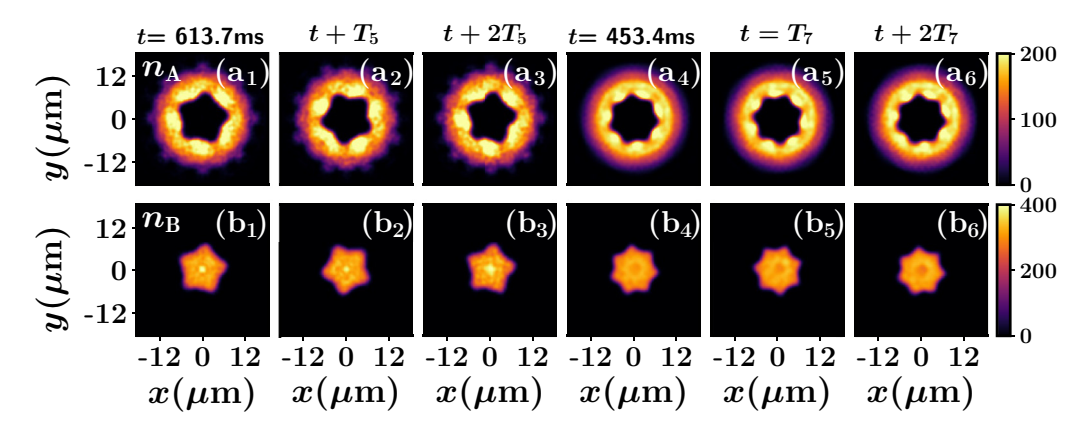


FIG. 4. Density snapshots of (a_1-a_6) species A and (b_1-b_6) species B for various symmetric patterns, D_5 [(a_1) , (a_2) , (a_3) ((b_1) , (b_2) , (b_3)] and D_7 [(a_4) , (a_5) , (a_6) , (b_4) , (b_5) , (b_6)], at selected instants in time (see legends) in the long-time dynamics. T_m is the driving period corresponding to the m-fold symmetric pattern D_m . To induce the dynamics, the trapping potential of species B is modulated with amplitude b = 0.24 and frequency $\omega_D = 2\pi/T_m$. The ⁸⁷Rb - ⁸⁵Rb binary BEC composed of $N_A = 10^4$ and $N_B = 5 \times 10^3$ atoms is initialized in its ground state with $a_{AA} = 99a_B$, $a_{AB} = 75a_B$, $a_{AB} = 213a_B$, and trap frequency $\omega_A = \omega_B = 2\pi \times 15$ Hz.

result, the assumptions made within the Floquet analysis are reasonably justified, at least for the calculation of the natural frequencies of the generated patterns.

V. PATTERN FORMATION IN A STRONGLY MASS-IMBALANCED MIXTURE

To expose the general character of our findings regarding the emergent star-shaped patterns building upon the interface of immiscible binary BECs, we next demonstrate as a case example the dynamics of the experimentally relevant strongly mass-imbalanced 41 K - 87 Rb mixture [89]. Before proceeding, it is also worth mentioning that the same pattern formation can also be generated in completely mass-balanced bosonic mixtures, e.g., by considering two hyperfine states of 87 Rb (not shown for brevity). Moreover, we have also performed the modulation dynamics using the particle number ratios $N_{\rm B}/N_{\rm A}=0.7,\ 0.85,\ {\rm and}\ 1$ and the trapping frequencies 10 and 25 Hz and found that these systems also show an overall phenomenology similar to those discussed in the previous sections

For simplicity, in the following we label ⁴¹K as species A and ⁸⁷Rb as species B with $m_r = m_A/m_B = 0.47$ and particle number in each component $N_A = 5 \times 10^3$ and $N_B =$ 5×10^3 . Moreover, we employ the experimentally realizable (for this mixture) values of the intra- and interspecies scattering lengths [90–92]. These correspond to $a_{AA} = 65a_{B}$ and $a_{\rm BR} = 99a_{\rm B}$ for the $^{41}{\rm K}$ and $^{87}{\rm Rb}$ atoms, respectively, while the interspecies one is fixed to the value $a_{AB} = 163a_{B}$. Also, we use a 2D harmonic oscillator potential of frequency ω_A = $\omega_{\rm B}=2\pi\times 15$ Hz. As before, the system is initially prepared in its immiscible ground state, where now the ⁸⁷Rb atoms (heavier species) configure the core condensate and the ⁴¹K atoms (lighter species) form a shell around it. To trigger the dynamics, we subsequently modulate the scattering length $a_{\rm BB}$ time-periodically with amplitude A and frequency ω_D according to the protocol $\tilde{a}_{BB} = a_{BB} + A \cos(\omega_D t)$. We also consider $A = 20a_{\rm B}$ such that the ratio $A/a_{\rm BB} \approx 0.2$ is the same as in Sec. III A. Let us also note in passing that a similar phenomenology regarding the generation of star-shaped patterns can be realized when modulating the scattering length of the shell condensate or the trapping potential of either species (not shown).

Characteristic density profiles of each species showcasing fivefold [Figs. $5(a_1)$ – $5(a_3)$ and Figs. $5(b_1)$ – $5(b_3)$] and sevenfold [Figs. $5(a_4)-5(a_6)$ and Figs. $5(b_4)-5(b_6)$] symmetric patterns are presented in Fig. 5 after applying the periodic driving of the 87Rb scattering length. More specifically, the abovementioned patterns are realized for driving frequencies $\omega_D =$ 73 Hz (D_5) and $\omega_D = 98$ Hz (D_7) , respectively. Of course, it is possible to dynamically create all the different m-fold patterns by using the appropriate driving frequencies. Remarkably, the patterns appearing in Fig. 5 feature a dynamics similar to that previously discussed, namely, a particular m-fold symmetric pattern D_m is repeated exactly at the same location at $t + 2T_m$ (where T_m is the time period of the driving), thus revealing its subharmonic nature. However, due to the significant mass imbalance the same patterns are realized at a different driving frequency compared to the sightly mass-imbalanced ⁸⁷Rb - ⁸⁵Rb scenario. This behavior is also supported by the $\omega_m(m)$ dispersion relation derived within the Floquet theory [see also the discussion following Eq. (7)]. Summarizing, according to our mean-field calculations we can deduce that the significant mass imbalance between the species affects the natural angular frequencies of the emergent patterns and the time scale of the appearance of the relevant phenomenology.

VI. CONCLUSIONS AND FUTURE CHALLENGES

The interface dynamics of a phase-separated binary BEC subjected to a periodic modulation of the core-component scattering length has been investigated using mean-field theory and a Floquet analysis. We have found that, depending on the driving frequency, the interface becomes unstable to azimuthal undulations. As a result of the instability, it is possible to controllably induce patterns of $m \geqslant 3$ -fold rotational symmetry in the immiscible two-component system and to predict their symmetries, as well as their subsequent time evolution and recurrence. Utilizing Floquet analysis we derived a dispersion relation which allows us to predict the

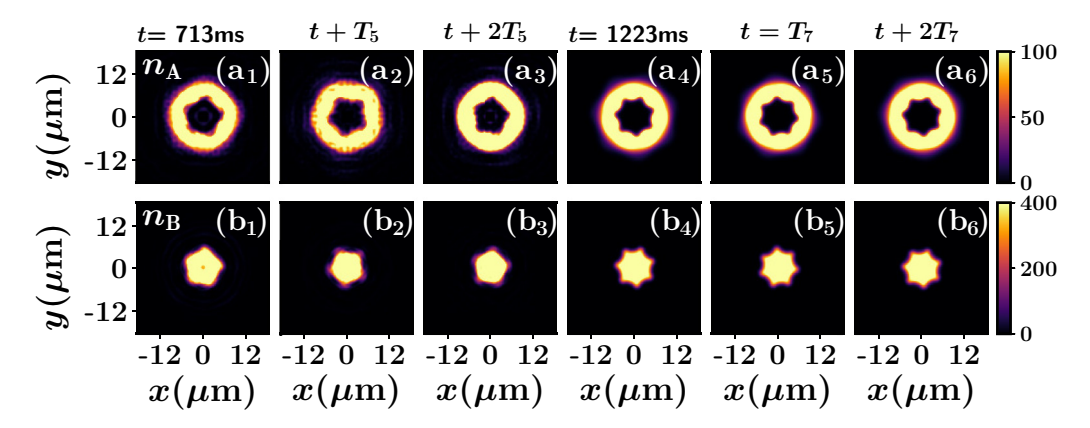


FIG. 5. Density profiles of (a_1-a_6) species A (^{41}K) and (b_1-b_6) species B (^{87}Rb) showing different symmetric patterns, namely, D_5 [(a_1) , (a_2) , (a_3) ((b_1) , (b_2) , (b_3)] and D_7 [(a_4) , (a_5) , (a_6) , (b_4) , (b_5) , (b_6)], at selected instants in time (see legends) of the long-time dynamics. T_m refers to the driving period corresponding to the m-fold symmetric pattern D_m . The dynamics is induced by a periodic modulation of the ^{87}Rb scattering length with amplitude $A = 20a_B$ and frequency $\omega_D = 2\pi/T_m$. The ^{41}K - ^{87}Rb binary BEC contains $N_A = 5 \times 10^3$ and $N_B = 5 \times 10^3$ atoms and it is prepared in its ground state with $a_{AA} = 65a_B$, $a_{BB} = 99a_B$, $a_{AB} = 163a_B$, and trapping frequency $\omega_A = \omega_B = 2\pi \times 15$ Hz.

natural frequencies of the emergent patterns. A close comparison between the predictions of the reduced description of the parametric resonance on the basis of the Mathieu equation and the mean-field GP framework reveals an adequate agreement between the two approaches as regards quantifying the relevant intervals of existence of specific patterns in terms of the driving frequencies and amplitudes. Most importantly, in cold-atom experiments, these patterns and the corresponding driving frequencies can be employed to determine the interfacial tension. We explicitly calculate the latter by combining our mean-field and Floquet theory predictions. Moreover, we have showcased that the interfacial pattern formation can also be triggered in strongly mass-imbalanced setups and by modulating the external trapping potential.

In the realm of two spatial dimensions, it would be intriguing to examine the corresponding instabilities and consequent pattern formation in the presence of dipolar as well as spin-orbit interactions or in the context of 2D quantum droplets [93]. The extension of our results to the highamplitude driving regime in order to characterize the corresponding pattern formation constitutes another interesting direction. Certainly, deriving an effective quasi-1D equation [94] characterizing the interface dynamical evolution, beyond the linearized stage considered herein, would be an interesting perspective. Moreover, to connect with experiments such as the one in [63], it would be relevant to extend considerations to a fully 3D setting. Finally, possible alterations of the emergent patterns caused by the inclusion of interparticle correlations [95–98] in the current setting would be relevant to consider.

ACKNOWLEDGMENTS

K.M. acknowledges a research fellowship (Funding ID No. 57381333) from the Deutscher Akademischer Austauschdienst (DAAD). S.I.M. gratefully acknowledges financial support in the framework of the Lenz-Ising Award of the University of Hamburg. K.M. thanks A. K. Mukhopadhyay for a careful reading of the manuscript and insightful discussions. This material is based on work supported by the

US National Science Foundation under Grants No. PHY-1602994 and No. DMS-1809074 (P.G.K.). P.G.K. also acknowledges support from the Leverhulme Trust via a Visiting Fellowship and thanks the Mathematical Institute of the University of Oxford for its hospitality during part of this work.

APPENDIX A: DIMENSIONAL REDUCTION AND COMPUTATIONAL DETAILS

Let us elaborate on how the full 3D GP equations of motion boil down to their 2D form used for the calculations presented in the text. The coupled set of full 3D GP equations, discussed in the text, can be cast into a dimensionless form by scaling the spatial coordinates as $x' = x/a_{osc}$, $y' = y/a_{osc}$, $z' = z/a_{osc}$, the time $t' = t/\omega_A$, and the wave function $\Psi'_i(x', y', z') =$ $\sqrt{a_{\rm osc}^3/N_j}\Psi_j(x,y,z,t)$. Here, the index j=A,B refers to each of the species of the binary BEC, while $a_{\rm osc} = \sqrt{\hbar/m\omega_{\rm A}}$ is the harmonic oscillator length. For convenience, in the following, we drop the prime sign and assume that the trapping frequency in the transverse x-y plane satisfies $\omega_A = \omega_B = \omega$. The quasi-2D harmonic trap is achieved by applying a much stronger trapping in the axial z direction compared to that along the x-y plane, i.e., $\omega_7 \gg \omega$. Therefore, under the condition $\lambda = (\omega_7/\omega) \gg 1$, the wave function of each species can be factorized as

$$\Psi_i(x, y, z, t) = \psi_i(x, y, t)\phi_i(z), \tag{A1}$$

where $\phi_j(z)$ is the normalized ground-state wave function in the z direction. Subsequently, the dimensionless form of the coupled GP equations after integrating over $\phi_j(z)$ results in the 2D form:

$$i\frac{\partial \psi_{A}(x,y,t)}{\partial t}$$

$$= \left[-\frac{1}{2}\nabla_{\perp}^{2} + \frac{1}{2}(x^{2} + y^{2}) + \sum_{j} \mathcal{G}_{Aj}|\psi_{j}(x,y)|^{2} \right] \psi_{A}(x,y,t)$$
(A2)

and

$$i\frac{\partial \psi_{B}(x,y,t)}{\partial t} = \left[-\frac{m_r}{2} \nabla_{\perp}^2 + \frac{1}{2m_r} (x^2 + y^2) + \sum_{j} \mathcal{G}_{Bj} |\psi_j(x,y)|^2 \right] \psi_{B}(x,y,t). \quad (A3)$$

In these expressions, $\nabla_{\perp}^2 = \partial_x^2 + \partial_y^2$ connects to the kinetic energy term and $m_r = m_{\rm A}/m_{\rm B}$. Furthermore, $\mathcal{G}_{\rm AA} = 2N_{\rm A}\sqrt{2\pi}\lambda a_{\rm AA}/a_{\rm osc}$ and $\mathcal{G}_{\rm BB} = 2m_rN_{\rm B}\sqrt{2\pi}\lambda a_{\rm BB}/a_{\rm osc}$ refer to the intraspecies interaction strengths, while $\mathcal{G}_{jj'} = N_{j'}(1+m_r)\sqrt{2\pi}\lambda a_{jj'}/a_{\rm osc}$ is the interspecies interaction strength.

Regarding our mean-field calculations presented in the text, we numerically solve the above-described GP equations [Eqs. (A2) and (A3)] using a split-time Crank-Nicolson method adapted for binary condensates [70-72]. The initial ground state of the binary system is obtained by propagating the relevant equations in imaginary time, until the solution converges to the desired state. Furthermore, the normalization of the j-species wave function is ensured by utilizing the transformation $\psi_j o \frac{\psi_j}{\|\psi_j\|}$ at every instant of the imaginarytime propagation until the energy of the desired configuration is reached with a precision of 10^{-8} . Having these solutions at hand as initial conditions, at t = 0, we study their evolution in real time. The corresponding simulations are performed within a square grid containing 400×400 grid points with a grid spacing $\Delta x = \Delta y = 0.05$. The time step of the integration Δt is chosen to be 10^{-4} .

APPENDIX B: DYNAMICAL EMERGENCE OF PATTERNS UPON MODULATING THE SCATTERING LENGTH OF THE SHELL CONDENSATE

In the text, the pattern formation on the immiscible BEC interface has been demonstrated by applying a periodic modulation of the scattering length $a_{\rm BB}$ of the core component consisting of $^{85}{\rm Rb}$ atoms. This particular parameter choice is especially motivated by the already demonstrated experimental feasibility of tuning the scattering length of $^{85}{\rm Rb}$ atoms by means of Feshbach resonances [64]. In the following, we argue that the above-described parametric instability phenomenon, being an azimuthal symmetry-breaking phenomenon, is quite generic for an immiscible condensate in the sense that it is manifested through the periodic driving of any of the involved intra- and interspecies scattering lengths.

To support our arguments we demonstrate that it is possible to dynamically generate the above-mentioned patterns following a time-periodic modulation of the *shell* condensate scattering length $a_{\rm AA}$. More specifically, we consider a binary bosonic mixture of ⁸⁷Rb - ⁸⁵Rb atoms, labeling ⁸⁷Rb (⁸⁵Rb) as species A (B). Both species are confined in a 2D isotropic harmonic trap with frequencies $\omega_{\rm A} = \omega_{\rm B} \equiv \omega = 2\pi \times 15$ Hz. The intra- and interspecies scattering lengths are chosen to be $a_{\rm BB} = 75 a_{\rm B}$, $a_{\rm AA} = 99 a_{\rm B}$, and $a_{\rm AB} = 213 a_{\rm B}$, while the two species contain, respectively, particle numbers $N_{\rm A} = 10^4$ and $N_{\rm B} = 5 \times 10^3$. Evidently, the initial state is the same as the one considered in the text, namely, the ⁸⁷Rb and the ⁸⁵Rb form the core and shell condensates, respectively. To trigger the

dynamics, we apply the modulation $\tilde{a}_{AA} = a_{AA} + \mathcal{A}\cos(\omega_D t)$ of the scattering length of the shell condensate. In particular, we consider $\mathcal{A} = 20a_B$ such that $\mathcal{A}/a_{AA} \approx 0.2$.

Characteristic density profiles of each species in the course of the time evolution are presented in Fig. 6, where the pattern formation occurring at the interface of the binary BEC is illustrated. In particular, as a case example, we showcase the dynamical formation of fourfold [Figs. $6(a_1)$ – $6(a_3)$ and Figs. $6(b_1)$ – $6(b_3)$] and sevenfold [Figs. $6(a_4)$ – $6(a_6)$ and Figs. 6(b₄)-6(b₆)] symmetric patterns following the periodic driving of the ⁸⁷Rb scattering length. These patterns are generated subharmonically, which is evident from their repetition at $t' = t + 2T_m$. The above-mentioned patterns are realized for driving frequencies $\omega_D = 69 \text{ Hz } (D_4)$ and $\omega_D = 168 \text{ Hz}$ (D_7) , respectively. We remark that also other patterns possessing a different m-fold symmetry can be formed within this protocol in the considered setting (results not shown for brevity). Finally, we mention in passing that the same overall phenomenology can be identified by considering the same setup (as in the text) but modulating the interspecies scattering length a_{AB} , namely, $\tilde{a}_{AB} = a_{AB} + A \cos(\omega_D t)$, e.g., with $A = 40a_B$. Remarkably, also in this case a variety of *m*-fold symmetric patterns can again be realized for distinct driving frequencies ω_D (not shown).

APPENDIX C: DERIVATION OF THE MATHIEU EQUATION

Here we discuss in detail the derivation of the Mathieu equation within the Floquet analysis [18,78–80] presented in the text. In particular, we start from a pair of 3D equations which are subsequently reduced to a form including only a single degree of freedom that is able to describe the emergent pattern formation in two dimensions. Following the Madelung transformation [83] of the condensate wave function, namely, $\Psi_j(r,\theta,z) = \sqrt{n_j(r,\theta,z)}e^{i\phi}$, with n_j and ϕ_j being the density and the phase of the j species and using the superfluid velocity $v_j = \frac{\hbar}{m_j} \nabla \phi_j$ [84], the hydrodynamic form of the GP equations regarding v_j is written

$$-m_{\rm A}\frac{\partial \mathbf{v}_{\rm A}}{\partial t} = \frac{\nabla P_{\rm A}}{n_{\rm A}}, \quad -m_{\rm B}\frac{\partial \mathbf{v}_{\rm B}}{\partial t} = \frac{\nabla P_{\rm B}}{n_{\rm B}}.$$
 (C1)

Integrating these equations we can easily show that the effective pressure terms of the species P_i satisfy

$$P_{\rm B} - P_{\rm A} = \hbar n_{\rm A} \frac{\partial \phi_{\rm A}}{\partial t} - \hbar n_{\rm B} \frac{\partial \phi_{\rm B}}{\partial t} + C, \tag{C2}$$

where C is an integration constant. Subsequently, we decompose the fluid pressure P_j into a so-called static part, $P_j^{\rm s}$, and a dynamical one, $P_j^{\rm d}$. In particular, before the onset of the patterns only the static pressure is present in the system, while both of them exist afterwards. Note that $P_j^{\rm s}$ can be obtained considering that the phase ϕ_j remains constant before the undulation of the interface starts, i.e., $\frac{\partial \phi_j}{\partial t} \approx 0$. Therefore considering that $P_{\rm A} = \frac{1}{2}(m_{\rm A}n_{\rm A}v_{\rm A}^2) + \frac{\hbar^2\sqrt{n_{\rm A}}}{2m_{\rm A}}\nabla^2\sqrt{n_{\rm A}} + g_{\rm AA}n_{\rm A}^2 + \frac{1}{2}m_{\rm A}n_{\rm A}\omega^2(r^2 + \lambda_{\rm A}^2z^2)$ and $P_{\rm B} = \frac{1}{2}(m_{\rm B}n_{\rm B}v_{\rm B}^2) + \frac{\hbar^2\sqrt{n_{\rm B}}}{2m_{\rm B}}\nabla^2\sqrt{n_{\rm B}} + g_{\rm BB}n_{\rm B}^2 + \frac{1}{2}m_{\rm B}n_{\rm B}\omega^2(r^2 + \lambda_{\rm BB}^2)$

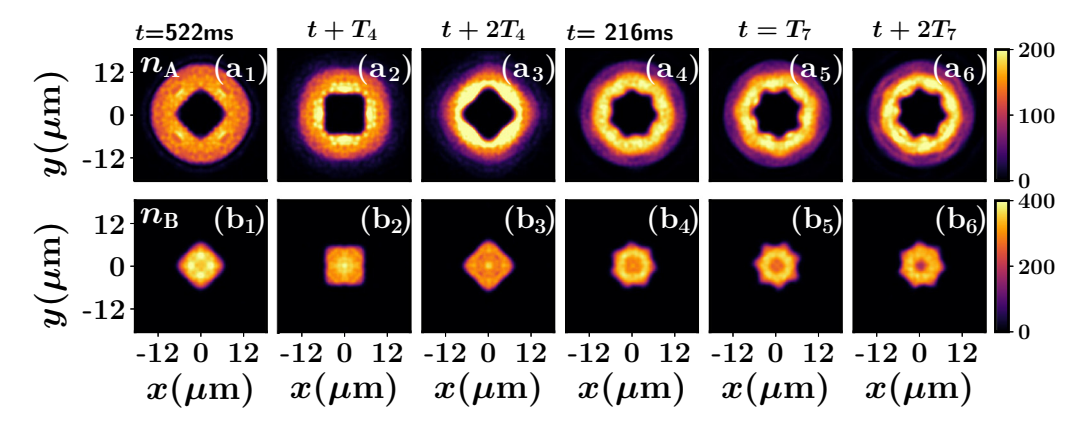


FIG. 6. Density profiles of (a_1-a_6) species A (^{87}Rb) and (b_1-b_6) species B (^{85}Rb) exhibiting different symmetric patterns, i.e., D_4 [(a_1) , (a_2) , (a_3) ((b_1) , (b_2) , (b_3)] and D_7 [(a_4) , (a_5) , (a_6) , (b_4) , (b_5) , (b_6)], at selected instants in time (see legends) of the long-time dynamics. T_m refers to the driving period in which the m-fold symmetric pattern D_m dynamically appears. The dynamics is triggered by a periodic modulation of the ^{87}Rb scattering length with amplitude $\mathcal{A}=20a_B$ and frequency $\omega_D=2\pi/T_m$. The $^{87}\text{Rb}-^{85}\text{Rb}$ binary BEC possesses $N_A=10^4$ and $N_B=5\times10^3$ atoms and it is initialized in its ground state with $a_{AA}=99a_B$, $a_{BB}=75a_B$, $a_{AB}=213a_B$, and trapping frequency $\omega_A=\omega_B=2\pi\times15\,\text{Hz}$.

 $\lambda_{\rm B}^2 z^2$)1 + $\frac{1}{2} m_{\rm B} n_{\rm B} \omega^2 r^2 b \cos(\omega_D t)$, it holds that

$$P_{\rm B}^{\rm s} - P_{\rm A}^{\rm s} = \frac{1}{2} m_{\rm B} \omega^2 n_{\rm B} r^2 b \cos(\omega_D t) + g_{\rm BB} n_{\rm B}^2 - g_{\rm AA} n_{\rm A}^2$$
. (C3)

To arrive at Eq. (C3) we have assumed that the background density is uniform and as a result the modulation of the harmonic potential impacts only the BEC interface. The constant $C' = g_{\rm BB} n_{\rm B}^2 - g_{\rm AA} n_{\rm A}^2$ can be found from the standard pressure jump condition at the interface [see also Eq. (4)]. For a cylindrical surface, which we have considered herein, $R_2 \to \infty$ and $R_1 \to R$. As a consequence,

$$[P_{\rm B}^{\rm s} - P_{\rm A}^{\rm s}]_{r=R} = \frac{1}{2} m_{\rm B} \omega^2 n_{\rm B} b R^2 \cos(\omega_D t) + C' = \frac{\sigma}{R},$$
 (C4)

which readily implies that

$$C' = -\frac{1}{2}m\omega_{\rm B}^2 n_{\rm B} b R^2 \cos(\omega_D t) + \frac{\sigma}{R}.$$
 (C5)

In this way, the difference in the static pressure term between the species is given by

$$P_{\rm B}^{\rm s} - P_{\rm A}^{\rm s} = \frac{1}{2} m_{\rm B} \omega^2 n_{\rm B} b (r^2 - R^2) \cos(\omega_D t) + \frac{\sigma}{R},$$
 (C6)

and accordingly the dynamical one acquires the form

$$P_{\rm B}^{\rm d} - P_{\rm A}^{\rm d} = \hbar n_{\rm A} \frac{\partial \phi_{\rm A}}{\partial t} - \hbar n_{\rm B} \frac{\partial \phi_{\rm B}}{\partial t}.$$
 (C7)

Furthermore, after the onset of the instability, the curved surface of the cylinder is deformed. Accordingly, for a deformed cylindrical surface with deformation ζ , the right-hand side of Eq. (4) can be linearized [85] as follows:

$$\sigma \left[\frac{1}{R_1} + \frac{1}{R_2} \right] = \frac{\sigma}{R} - \sigma \left[\frac{1}{R^2} + \frac{1}{R^2} \frac{\partial^2}{\partial \theta^2} + \frac{\partial^2}{\partial z^2} \right] \zeta. \quad (C8)$$

Moreover, the left-hand-side of Eq. (4) can be linearized around r = R (using the Taylor series expansion) as

$$[P_{\rm B} - P_{\rm A}]_{r=R+\zeta} = \frac{\sigma}{R} + n_{\rm B} m_{\rm B} \omega^2 b R \cos(\omega_D t) \zeta$$
$$+ \hbar n_{\rm A} \frac{\partial \phi_{\rm A}}{\partial t} - \hbar n_{\rm B} \frac{\partial \phi_{\rm B}}{\partial t}. \tag{C9}$$

Equating Eq. (C8) and Eq. (C9) at r = R we then get

$$\hbar n_{\rm A} \frac{\partial \phi_{\rm A}}{\partial t} - \hbar n_{\rm B} \frac{\partial \phi_{\rm B}}{\partial t} = -m_{\rm B} \omega^2 n_{\rm B} b R \cos(\omega_D t) \zeta
- \sigma \left[\frac{1}{R^2} + \frac{1}{R^2} \frac{\partial^2}{\partial \theta^2} + \frac{\partial^2}{\partial z^2} \right] \zeta.$$
(C10)

Let us then write the deformation $\zeta(r, \theta, z, t)$ in the form

$$\zeta(\theta, z, t) = \sum_{m=1}^{\infty} \zeta_m(t) e^{i(m\theta + kz)}.$$
 (C11)

Furthermore, the phase terms ϕ_A and ϕ_B following the solution of the Laplace equation [99] $\nabla^2 \phi_j = 0$ can be expressed as

$$\phi_{A}(r,\theta,z,t) = \sum_{m=1}^{\infty} \mathcal{P}K_{m}(kr)e^{i(m\theta+kz)}$$
 (C12)

and

$$\phi_{\rm B}(r,\theta,z,t) = \sum_{m=1}^{\infty} \mathcal{Q}I_m(kr)e^{i(m\theta+kz)}, \qquad (C13)$$

where $I_m(kr)$ and $K_m(kr)$ denote the *m*th-order modified Bessel functions of the first and second kind, respectively [86]. Also, \mathcal{P} and \mathcal{Q} are constants while the integers m and k are the azimuthal and axial wave numbers, respectively.

The kinematic boundary condition is defined as [85]

$$\frac{\partial \zeta}{\partial t} = v_{\text{Ar}}(r = R) = v_{\text{Br}}(r = R).$$
 (C14)

Employing Eq. (C14)we arrive at

$$\frac{d\zeta_m(t)}{dt} = \frac{\hbar k}{m_{\rm A}} \mathcal{P} K'_m(kR) = \frac{\hbar k}{m_{\rm B}} \mathcal{Q} I'_m(kR). \tag{C15}$$

Consequently, \mathcal{P} and \mathcal{Q} can be obtained from Eq. (C15). Then, by utilizing Eqs. (C12) and (C13), we can write the phase of species A as

$$\phi_{A}(r,\theta,z,t) = \sum_{m=1}^{\infty} \frac{d\zeta_{m}(t)}{dt} \frac{m_{A}K_{m}(kr)}{\hbar kK'_{m}(kR)} e^{i(m\theta+kz)}$$
(C16)

and that of species B as

$$\phi_{\rm B}(r,\theta,z,t) = \sum_{m=1}^{\infty} \frac{d\zeta_m(t)}{dt} \frac{m_{\rm B} I_m(kr)}{\hbar k I'_m(kR)} e^{i(m\theta + kz)}.$$
 (C17)

Substituting Eqs. (C16) and (C17) into Eq. (C10), we get

$$\sum_{m=1}^{\infty} \left[n_{A} m_{A} \frac{K_{m}(kR)}{kK'_{m}(kR)} \frac{d^{2} \zeta_{m}}{dt^{2}} - n_{B} m_{B} \frac{I_{m}(kR)}{kI'_{m}(kR)} \frac{d^{2} \zeta_{m}}{dt^{2}} \right] e^{i(m\theta + kz)}$$

$$= \sum_{m=1}^{\infty} \left[-m_{B} \omega^{2} R n_{B} b \cos(\omega_{D} t) + \sigma \left(\frac{m^{2} - 1}{R^{2}} + k^{2} \right) \right] \zeta_{m} e^{i(m\theta + kz)}. \tag{C18}$$

Next we let $k \to 0$ and use $\lim_{k \to 0} \frac{K_m(kR)}{kK'_m(kR)} = \lim_{k \to 0} \frac{I_m(kR)}{kI'_m(kR)} = \frac{R}{m}$ to arrive at

$$\frac{d^{2}\zeta_{m}}{dt^{2}} + \frac{\sigma m(m^{2} - 1)}{R^{3}(m_{B}n_{B} - m_{A}n_{A})} \times \left[1 - \frac{m_{B}\omega^{2}n_{B}R^{3}b}{\sigma(m^{2} - 1)}\cos(\omega_{D}t)\right]\zeta_{m} = 0.$$
(C19)

- Equation (C19) has the form of the so-called Mathieu equation used in the text. Note that Eq. (C19) possesses only one degree of freedom, i.e., ζ_m , which is the amplitude (associated with the radial direction) of the mth mode (related to the azimuthal direction), thus highlighting the 2D nature of the patterns. Moreover, the choice of $k \to 0$ indicates the absence of wave excitations along the z direction. The latter ensures that the dynamics of the system is "frozen" in the z direction. Recall that we have also utilized this approximation in order to reduce the full 3D GP equations of motion into 2D ones. Another important observation is that the parameters R, $n_{\rm B}$, and $n_{\rm A}$ determine the natural angular frequencies of the emergent patterns, while the values of these parameters used within the Floquet analysis are taken from the initial state obtained via the full GP calculations. Hence even though the interspecies interaction g_{AB} does not explicitly appear in the relevant equations of the Floquet analysis, its effect is implicitly included in the values of R, $n_{\rm B}$, and $n_{\rm A}$. In other words, any modification of g_{AB} in the initial state of the binary BEC would definitely shift the natural angular frequencies of the patterns, since it alters the magnitude of R, $n_{\rm B}$, and n_A . For instance, if g_{AB} is increased, then R decreases and consequently $n_{\rm B}$ increases, leading in turn to a modification of the respective natural angular frequency ω_m [see also the discussion below Eq. (7) in the text].
- [1] X. Noblin, A. Buguin, and F. Brochard-Wyart, Phys. Rev. Lett. **94**, 166102 (2005).
- [2] P. Brunet and J. H. Snoeijer, Eur. Phys. J.: Spec. Top. 192, 207 (2011).
- [3] C. L. Shen, W. J. Xie, and B. Wei, Phys. Rev. E **81**, 046305 (2010).
- [4] R. J. A. Hill and L. Eaves, Phys. Rev. E **81**, 056312 (2010).
- [5] M. Faraday, Philos. Trans. R. Soc. London 121, 299 (1831).
- [6] A. Adou and L. Tuckerman, J. Fluid Mech. 805, 591 (2016).
- [7] Y. Li, P. Zhang, and N. Kang, Phys. Fluids 30, 102104 (2018).
- [8] D. K. Maity, K. Kumar, and S. P. Khastgir, Exp. Fluids 61, 25 (2020).
- [9] D. K. Maity, arXiv:1912.04688 [physics.flu-dyn].
- [10] W. S. Edwards and S. Fauve, J. Fluid Mech. 278, 123 (1994).
- [11] K. Kumar, Proc. R. Soc. Lond. A 452, 1113 (1996).
- [12] R. Takaki and K. Adachi, J. Phys. Soc. Jpn. 54, 2462 (1985).
- [13] S. Douady, J. Fluid Mech. 221, 383 (1990).
- [14] C. Chin, R. Grimm, P. Julienne, and E. Tiesinga, Rev. Mod. Phys. 82, 1225 (2010).
- [15] T. Köhler, K. Góral, and P. S. Julienne, Rev. Mod. Phys. 78, 1311 (2006).
- [16] I. Bloch, J. Dalibard, and W. Zwerger, Rev. Mod. Phys. 80, 885 (2008).
- [17] J. J. García-Ripoll, V. M. Pérez-García, and P. Torres, Phys. Rev. Lett. 83, 1715 (1999).
- [18] K. Staliunas, S. Longhi, and G. J. de Valcárcel, Phys. Rev. Lett. 89, 210406 (2002).
- [19] R. Nath and L. Santos, Phys. Rev. A 81, 033626 (2010).

- [20] A. Balaž, R. Paun, A. I. Nicolin, S. Balasubramanian, and R. Ramaswamy, Phys. Rev. A 89, 023609 (2014).
- [21] M. Modugno, C. Tozzo, and F. Dalfovo, Phys. Rev. A 74, 061601(R) (2006).
- [22] A. I. Nicolin, R. Carretero-González, and P. G. Kevrekidis, Phys. Rev. A 76, 063609 (2007).
- [23] S. E. Pollack, D. Dries, R. G. Hulet, K. M. F. Magalhães, E. A. L. Henn, E. R. F. Ramos, M. A. Caracanhas, and V. S. Bagnato, Phys. Rev. A 81, 053627 (2010).
- [24] P. Engels, C. Atherton, and M. A. Hoefer, Phys. Rev. Lett. 98, 095301 (2007).
- [25] J. H. V. Nguyen, M. C. Tsatsos, D. Luo, A. U. J. Lode, G. D. Telles, V. S. Bagnato, and R. G. Hulet, Phys. Rev. X 9, 011052 (2019).
- [26] H. Saito and M. Ueda, Phys. Rev. Lett. 90, 040403 (2003).
- [27] F. K. Abdullaev, J. G. Caputo, R. A. Kraenkel, and B. A. Malomed, Phys. Rev. A 67, 013605 (2003).
- [28] P. G. Kevrekidis, G. Theocharis, D. J. Frantzeskakis, and B. A. Malomed, Phys. Rev. Lett. 90, 230401 (2003).
- [29] K. Staliunas, S. Longhi, and G. J. de Valcárcel, Phys. Rev. A 70, 011601(R) (2004).
- [30] V. R. Kumar, R. Radha, and P. K. Panigrahi, Phys. Rev. A 77, 023611 (2008).
- [31] A. I. Nicolin, Phys. Rev. E 84, 056202 (2011).
- [32] T. Chen and B. Yan, Phys. Rev. A 98, 063615 (2018).
- [33] A. Balaž and A. I. Nicolin, Phys. Rev. A 85, 023613 (2012).
- [34] K. Łakomy, R. Nath, and L. Santos, Phys. Rev. A **86**, 023620 (2012).

- [35] F. K. Abdullaev, M. Ögren, and M. P. Sørensen, Phys. Rev. A 87, 023616 (2013).
- [36] G. Li, Phys. Rev. A 93, 013837 (2016).
- [37] T. Chen, K. Shibata, Y. Eto, T. Hirano, and H. Saito, Phys. Rev. A 100, 063610 (2019).
- [38] M. Trippenbach, K. Góral, K. Rzazewski, B. Malomed, and Y. B. Band, J. Phys. B: At. Mol. Opt. Phys 33, 4017 (2000).
- [39] R. A. Barankov, Phys. Rev. A 66, 013612 (2002).
- [40] K. L. Lee, N. B. Jørgensen, I.-K. Liu, L. Wacker, J. J. Arlt, and N. P. Proukakis, Phys. Rev. A 94, 013602 (2016).
- [41] J. O. Indekeu, C.-Y. Lin, N. Van Thu, B. Van Schaeybroeck, and T. H. Phat, Phys. Rev. A **91**, 033615 (2015).
- [42] K. Sasaki, N. Suzuki, D. Akamatsu, and H. Saito, Phys. Rev. A 80, 063611 (2009).
- [43] D. Kobyakov, V. Bychkov, E. Lundh, A. Bezett, V. Akkerman, and M. Marklund, Phys. Rev. A 83, 043623 (2011).
- [44] T. Kadokura, T. Aioi, K. Sasaki, T. Kishimoto, and H. Saito, Phys. Rev. A **85**, 013602 (2012).
- [45] K. Sasaki, N. Suzuki, and H. Saito, Phys. Rev. A 83, 053606 (2011).
- [46] J. O. Indekeu, N. Van Thu, C.-Y. Lin, and T. H. Phat, Phys. Rev. A 97, 043605 (2018).
- [47] H. Takeuchi, N. Suzuki, K. Kasamatsu, H. Saito, and M. Tsubota, Phys. Rev. B **81**, 094517 (2010).
- [48] N. Suzuki, H. Takeuchi, K. Kasamatsu, M. Tsubota, and H. Saito, Phys. Rev. A 82, 063604 (2010).
- [49] A. W. Baggaley and N. G. Parker, Phys. Rev. A 97, 053608 (2018).
- [50] A. Bezett, V. Bychkov, E. Lundh, D. Kobyakov, and M. Marklund, Phys. Rev. A 82, 043608 (2010).
- [51] C. K. Law, C. M. Chan, P. T. Leung, and M.-C. Chu, Phys. Rev. A **63**, 063612 (2001).
- [52] V. I. Yukalov and E. P. Yukalova, Laser Phys. Lett. 1, 50 (2004).
- [53] H. Takeuchi, S. Ishino, and M. Tsubota, Phys. Rev. Lett. 105, 205301 (2010).
- [54] C. Hamner, J. J. Chang, P. Engels, and M. A. Hoefer, Phys. Rev. Lett. 106, 065302 (2011).
- [55] H. Saito, Y. Kawaguchi, and M. Ueda, Phys. Rev. Lett. 102, 230403 (2009).
- [56] K. Sasaki, N. Suzuki, and H. Saito, Phys. Rev. Lett. 104, 150404 (2010).
- [57] K. Sasaki, N. Suzuki, and H. Saito, Phys. Rev. A 83, 033602 (2011).
- [58] S. Gautam and D. Angom, Phys. Rev. A 81, 053616 (2010).
- [59] D. Kobyakov, A. Bezett, E. Lundh, M. Marklund, and V. Bychkov, Phys. Rev. A 85, 013630 (2012).
- [60] D. Kobyakov, V. Bychkov, E. Lundh, A. Bezett, and M. Marklund, Phys. Rev. A 86, 023614 (2012).
- [61] B. Van Schaeybroeck, Phys. Rev. A 78, 023624 (2008).
- [62] I. E. Mazets, Phys. Rev. A 65, 033618 (2002).
- [63] K. M. Mertes, J. W. Merrill, R. Carretero-González, D. J. Frantzeskakis, P. G. Kevrekidis, and D. S. Hall, Phys. Rev. Lett. 99, 190402 (2007).
- [64] S. B. Papp, J. M. Pino, and C. E. Wieman, Phys. Rev. Lett. 101, 040402 (2008).
- [65] See Supplemental Material at http://link.aps.org/supplemental/ 10.1103/PhysRevA.102.033320 for movies depicting the for-

- mation of various symmetric patterns such as D_3 , D_4 , D_5 , D_6 , and D_7 .
- [66] C. J. Pethick and H. Smith, Bose-Einstein Condensation in Dilute Gases (Cambridge University Press, Cambridge, UK, 2002).
- [67] S. Stringari and L. Pitaevskii, Bose-Einstein Condensation (Oxford University Press, Oxford, UK, 2003).
- [68] P. Ao and S. T. Chui, Phys. Rev. A 58, 4836 (1998).
- [69] E. Timmermans, Phys. Rev. Lett. 81, 5718 (1998).
- [70] P. Muruganandam and S. Adhikari, Comput. Phys. Commun. 180, 1888 (2009).
- [71] D. Vudragović, I. Vidanović, A. Balaž, P. Muruganandam, and S. K. Adhikari, Comput. Phys. Commun. 183, 2021 (2012).
- [72] K. Mukherjee, S. I. Mistakidis, P. G. Kevrekidis, and P. Schmelcher, J. Phys. B: At. Mol. Opt. Phys. 53, 055302 (2020).
- [73] S. B. Papp and C. E. Wieman, Phys. Rev. Lett. 97, 180404 (2006).
- [74] N. R. Claussen, S. J. J. M. F. Kokkelmans, S. T. Thompson, E. A. Donley, E. Hodby, and C. E. Wieman, Phys. Rev. A 67, 060701(R) (2003).
- [75] M. Erhard, H. Schmaljohann, J. Kronjäger, K. Bongs, and K. Sengstock, Phys. Rev. A 69, 032705 (2004).
- [76] Z. Zhang, K.-X. Yao, L. Feng, J. Hu, and C. Chin, Nat. Phys 16, 652 (2020).
- [77] D. S. Hall, M. R. Matthews, J. R. Ensher, C. E. Wieman, and E. A. Cornell, Phys. Rev. Lett. 81, 1539 (1998).
- [78] N. Goldman and J. Dalibard, Phys. Rev. X 4, 031027 (2014).
- [79] S. R. Barone, M. A. Narcowich, and F. J. Narcowich, Phys. Rev. A 15, 1109 (1977).
- [80] A. Eckardt, Rev. Mod. Phys. 89, 011004 (2017).
- [81] S. Inouye, J. Goldwin, M. L. Olsen, C. Ticknor, J. L. Bohn, and D. S. Jin, Phys. Rev. Lett. 93, 183201 (2004).
- [82] R. Grimm, M. Weidemüller, and Y. B. Ovchinnikov, Adv. At. Mol. Opt. Phys. 42, 95 (2000).
- [83] E. Madelung, Z. Phys. 40, 322 (1927).
- [84] C. J. Pethick and H. Smith, Bose-Einstein Condensation in Dilute Gases, 2nd ed. (Cambridge University Press, Cambridge, UK, 2008).
- [85] H. Lamb, in *Hydrodynamics*, 6th ed. (Cambridge University Press, Cambridge, UK, 1932), pp. 55–68.
- [86] M. Abramowitz, Appl. Math. Ser. 55, 232 (1964).
- [87] L. Rayeligh, Proc. R. Soc. London 29, 71 (1879).
- [88] The error $\pm 5\%$ refers to the relative deviation of the value of σ obtained for different m's as predicted by the GP calculations.
- [89] G. Modugno, M. Modugno, F. Riboli, G. Roati, and M. Inguscio, Phys. Rev. Lett. 89, 190404 (2002).
- [90] A. Marte, T. Volz, J. Schuster, S. Dürr, G. Rempe, E. G. M. van Kempen, and B. J. Verhaar, Phys. Rev. Lett. 89, 283202 (2002).
- [91] H. Wang, A. N. Nikolov, J. R. Ensher, P. L. Gould, E. E. Eyler, W. C. Stwalley, J. P. Burke, J. L. Bohn, C. H. Greene, E. Tiesinga, C. J. Williams, and P. S. Julienne, Phys. Rev. A 62, 052704 (2000).
- [92] F. Ferlaino, C. D'Errico, G. Roati, M. Zaccanti, M. Inguscio, G. Modugno, and A. Simoni, Phys. Rev. A 73, 040702(R) (2006).
- [93] M. N. Tengstrand, P. Stürmer, E. O. Karabulut, and S. M. Reimann, Phys. Rev. Lett. 123, 160405 (2019).
- [94] P. G. Kevrekidis, W. Wang, R. Carretero-González, and D. J. Frantzeskakis, Phys. Rev. Lett. 118, 244101 (2017).

- [95] G. C. Katsimiga, S. I. Mistakidis, G. M. Koutentakis, P. G. Kevrekidis, and P. Schmelcher, New J. Phys. 19, 123012 (2017).
- [96] G. C. Katsimiga, G. M. Koutentakis, S. I. Mistakidis, P. G. Kevrekidis, and P. Schmelcher, New J. Phys. 19, 073004 (2017).
- [97] S. I. Mistakidis, G. C. Katsimiga, P. G. Kevrekidis, and P. Schmelcher, New J. Phys. 20, 043052 (2018).
- [98] K. Mukherjee, S. I. Mistakidis, S. Majumder, and P. Schmelcher, Phys. Rev. A 101, 023615 (2020).
- [99] J. D. Jackson, *Classical Electrodynamics* (John Wiley & Sons, New York, 2007).